First-principles calculations of the adsorption and hydrogenation reactions of $CH_x(x=0,4)$ species on a Fe(100) surface

D. C. Sorescu
U.S. Department of Energy, National Energy Technology Laboratory, Pittsburgh, Pennsylvania 15236, USA
(Received 28 December 2005; revised manuscript received 6 March 2006; published 18 April 2006)

A previous set of investigations related to adsorption, diffusion, and dissociation properties of CO [D. C. Sorescu, D. L. Thompson, M. M. Hurley, and C. F. Chabalowski, Phys. Rev. B **66**, 035416 (2002)] and H_2 [D. C. Sorescu, Catal. Today **105**, 44 (2005)] on Fe(100) surface have been extended to the case of chemisorption properties of CH_x $(x=0,4)$ species on the same surface. Similar to our previous studies, the current work is based on first-principles plane-wave calculations using spin-polarized density functional theory (DFT) and the generalized gradient approximation (GGA). The calculations employ slab geometry and periodic boundary conditions. It was determined that CH_x $(x=0,2)$ species preferentially adsorb at the four-folded sites while the CH_3 species prefer the binding at the bridge site. In contradistinction, the CH_4 molecule is only weakly physisorbed on the surface, independent of surface site or molecular orientation. In the case of the C atom, the adsorption investigations have been extended to include both the coverage effects as well as the possibility for absorption at subsurface sites. The presence of the C atom at either hollow or subsurface sites was found to increase the stability of the other atomic (C, H, O) and molecular or radical species [CO, CH_x $(x=1,4)$] adsorbed on the surface. Beside chemisorption properties, the activation energies for surface diffusion have been determined for all individual CH_x $(x=0,3)$species while in the case of C atom diffusion to subsurface sites have also been considered. Finally, we have determined the minimum energy path for the elementary hydrogenation reactions of CH_x $(x=0,3)$ species. We found that for the ensemble of surface processes involving dissociation of CO and H_2 on Fe(100) surface followed by hydrogenation of CH_x $(x=0,3)$ species with formation of CH_4, the CO dissociation is the rate determining step with an activation energy of 24.5 kcal/mol.

DOI: 10.1103/PhysRevB.73.155420 PACS number(s): 68.43.Fg, 31.15.Ew, 68.47.De, 82.37.Np

I. INTRODUCTION

Understanding the interactions of simple molecular systems like CO, H_2, and CH_x $(x=1,4)$ hydrocarbon species with iron surfaces is of primary importance as these systems can be involved in many catalytic processes such as methanation or Fischer-Tropsch (FT) synthesis of aliphatic hydrocarbons.[1–3] In the particular case of FT synthesis, there are several important issues that continue to receive scientific attention. Among these, achieving a chemical understanding of FT processes by identification of primary and secondary reaction steps as function of external reaction conditions is one of primary goals.[3] In the case of iron catalysts, the complexity of the mechanism is further increased due to the fact that the composition and the structure of the catalyst change following the initial decomposition of CO molecules.

The analysis of the adsorption and dissociation properties of CO and H_2 species on single crystal iron surfaces has been considered in several previous experimental studies.[4–8] Additionally, important steps toward an accurate atomistic description of the interaction of simple molecular systems such as CO and H_2 and of the corresponding atomic C, O, and H species with various iron surfaces have been taken in recent years through the use of first-principles calculations. Both cluster models and periodic supercell models in conjunction with density functional theory (DFT) calculations have been used to describe the adsorption properties of molecular CO on Fe(100) (Refs. 9 and 10) and Fe(110) (Refs. 11 and 12) surfaces, the interaction of atomic H,[13–15] O,[10,16] or C (Refs. 10 and 17) species with these surfaces or with bulk bcc Fe.

In the current study, we further expand our previous work[10,15] to include the analysis of chemisorption properties of CH_x $(x=1,4)$ species on Fe(100) surface as well as the early hydrogenation steps of these species. Obtaining the relative stabilities of various intermediates involved in the early steps of Fischer-Tropsch or methanol synthesis and understanding the potential energy surface leading to their formation has received significant attention in the case of other catalysts such as Ru,[18,19] Pd,[20] or Co.[21] Very recently a direct comparison of the early Fischer-Tropsch steps on Fe(110) and Co(0001) surfaces has been communicated by Mavrikakis and Gokhale.[22]

The organization of the paper is as follows: In Sec. II, we describe the computational methods used in this study. The results of total energy calculations for adsorption and diffusion properties of CH_x $(x=0,4)$ species and for the corresponding hydrogenation reactions are presented in Sec. III. Finally, we summarize the main conclusions in Sec. IV.

II. COMPUTATIONAL METHOD

The calculations performed in this study were done using the Vienna *ab initio* simulation package (Vasp). [23–25] This program evaluates the total energy of periodically repeating geometries based on density functional theory and the pseudopotential approximation. In this case the electron-ion interaction is described by fully nonlocal optimized ultrasoft

pseudopotentials (USPPs) similar to those introduced by Vanderbilt.[26,27] These USPPs include nonlinear core corrections to account for possible valence-core charge interactions due to the $3d$ valence states overlapping with the $3p$ semicore states in iron.[28] Calculations were performed using the spin polarized generalized gradient approximation (GGA) with the PW91 exchange-correlation functional of Perdew *et al.*[29] In the rest of the paper, we will refer to this computational method as USPP-PW91.

For comparison, we checked the accuracy of the main USPP results against the projector augmented wave (PAW) method of Blöchl[30] in the implementation of Kresse and Joubert.[31] This method which is an all-electron DFT technique within the frozen core approximation is known to improve the description of magnetic transition metals.[31] In this case we have also included the spin interpolation for the correlation energy proposed by Vosko-Wilk-Nusair (VWN).[32] Moreover, the effect of using a different exchange-correlation functional on the adsorption energies and activation energies of hydrogenation has also been investigated by using the Perdew, Burke, and Ernzerhof (PBE) functional.[33] In the rest of the paper, this method will be abbreviated as PAW-PBE.

The surface and the adsorbate-surface systems have been simulated using a slab model. Periodic boundary conditions are used, with the one electron pseudo-orbitals expanded over a plane-wave basis set. The expansion includes all plane waves with kinetic energy $\hbar^2k^2/2m < E_{cut}$, where k is the wave vector, m the electronic mass, and E_{cut} is the cutoff energy. The corresponding cutoff energies were chosen sufficiently large to ensure the convergence with respect to the basis set. The corresponding values were 495 eV in the case of USPPs and 400 eV for PAW calculations, respectively.

The sampling of the Brillouin zone was performed using a Monkhorst-Pack scheme.[34] Electron smearing was employed via the Methfessel-Paxton technique,[35] with a smearing width consistent with $\sigma=0.1$ eV, in order to minimize the errors in the Hellmann-Feynman forces due to the entropic contribution to the electronic free energy.[24,25] All energies were extrapolated to $T=0$ K. The minimization of the electronic free energy was performed using an efficient iterative matrix-diagonalization routine based on a sequential band-by-band residuum minimization method[24,25] (RMM) or alternatively based on preconditioned band-by-band conjugate-gradient (CG) minimization.[36] The optimization of different atomic configurations was performed by conjugate-gradient minimization of the total energy.

In a number of instances, we evaluated the vibrational frequencies of adsorbed molecular or radical species. This has been done under the frozen phonon mode approximation in which the metal atoms are fixed at the relaxed geometries. The Hessian matrix has been determined based on a finite difference approach with a step size of 0.02 Å for the displacements of the individual atoms of the adsorbate along each Cartesian coordinate. By diagonalization of the mass-weighted Hessian matrix, the corresponding frequencies and normal modes have been determined.

Evaluation of the activation energies for diffusion or hydrogenation processes of CH_x species has been done using the nudged elastic band (NEB) method of Jónsson and Mills.[37] In this approach, the reaction path is "discretized," with the discrete configurations, or images, between minima being connected by elastic springs to prevent the images from sliding to the minima in the optimization.

Based on a k-point mesh of $15\times15\times15$, we have determined the optimized equilibrium constant for bulk bcc iron as 2.865 Å at USPP-PW91, 2.831 Å at PAW-PW91, and 2.833 Å at PAW-PBE levels, respectively. The corresponding bulk modulus B_0 was found to be 1.597 Mbar at USPP-PW91, 1.73 Mbar at PAW-PW91, and 1.71 Mbar at PAW-PBE, respectively. These values compare well with experimental values of 2.87 Å and 1.68 Mbar, respectively.[38] At the optimized structure, the saturation magnetization at respective computational levels is 1844.4 Gs (USPP-PW91), 1790 Gs (PAW-PW91), and 1791 Gs (PAW-PBE). When comparing these values against the experimental data of 1750 Gs,[38] it is clear that both PAW-PW91 and PAW-PBE methods slightly improve the agreement with experiment for the saturation magnetization relative to the USPP-PW91 result. The detailed analysis of the structural relaxations obtained using the USPP and PAW methods were done before[10,15] and will not be repeated in the current work.

In our previous studies,[10,15] we have also shown that the current plane-wave DFT computational method can provide also an accurate description of the structural and energetic properties of CO and H_2 molecular systems. In this work, we provide further evidence of the accuracy of the plane-wave DFT method at both the USPP-PW91 and PAW-PBE levels for the case of CH_x $(x=1,4)$ molecular species. These investigations have been done by optimizing isolated CH_x $(x=1,4)$ species in a cubic box of 10 Å sides. The corresponding results for specific bond distances and angles, vibrational frequencies, and bond dissociation energies are compared in Table I with the corresponding experimental data. As can be seen from data presented in Table I, there is a reasonable good agreement among theoretical predictions at both PW91 and PBE levels and the corresponding experimental data.

Based on these and our previous[10,15] tests, it can be concluded that the current computational method is able to provide an accurate description of the structural and energetic properties of bulk Fe, the bare surface, and of the isolated CH_x $(x=1,4)$ species relative to the corresponding experimental values. These characteristics make us confident to pursue the next step of our investigations, namely interaction of CH_x species with Fe(100) surfaces.

III. RESULTS AND DISCUSSION

Characterization of the chemisorption properties of adsorbate species $[CH_x$ $(x=0,4)]$ on the Fe(100) surface has been performed using a 2×2 slab model with six layers containing a total of 24 Fe atoms. For the most stable configurations identified in this set of calculations, we have also analyzed the effect of even lower coverages using a larger 3×3 six-layer supercell with 58 Fe atoms. In both these cases, adsorption on a single side of the slab has been considered. The optimizations have been performed by relaxing the coordinates of the adsorbate species and of the Fe atoms in the first

TABLE I. Comparison of the calculated geometric parameters, vibrational frequencies and molecular bond dissociation energies of the isolated CH_x ($x=1,4$) species with experimental data.[a] The results are given for USPP-PW91 (Calc1) and PAW-PBE (Calc2) theoretical methods used in this study.

Species		r(C–H)	θ(H–C–H)	ν_1	ν_2	ν_3	ν_4	D_0
CH	Calc1	1.133	…	2774				83.3
	Calc2	1.138		2752				81.4
	Exp.[b]	1.120	…	2858 (Σ)				79.9±0.1
								80.9±0.2
CH_2	Calc1	1.082	135.2	3324	3082	1003		103.4
	Calc2	1.086	135.1	3313	3076	1015		104.1
	Exp.	1.078	130.0	3190 (B_2)	2806 (A_1)	963 (A_1)		100.4±0.1
								101.3±0.3
CH_3	Calc1	1.083	120.0	3247	3064	1362	542	107.2
	Calc2	1.087	120.0	3234	3054	1356	527	106.9
	Exp.	1.08	120.0	3161 (E')	3044 (A_1')	1396 (E')	606 (A_2'')	108.8±0.6
								110.4±0.2
CH_4	Calc1	1.094	109.47	3099	2984	1516	1295	101.7
	Calc2	1.097	109.47	3091	2973	1510	1284	101.8
	Exp.	1.087	109.47	3019 ($T2$)	2917 ($A1$)	1534 (E)	1306 ($T2$)	103.2±0.1
								104.9±0.03

[a]Bond distances are given in angstroms, bond angles in degrees, vibrational frequencies in cm^{-1}, and bond dissociation energies in kcal/mol. For experimental vibrations, the symmetry of specific eigenmodes is also provided in parentheses.

[b]The experimental geometric parameters and vibrational frequencies are taken from Ref. 39; while molecular bond dissociation energies are taken from Ref. 40.

two layers of the slab. The remaining atoms of the slab have been frozen at the bulk optimized positions.

The adsorption energies calculated throughout this work were obtained based on the expression

$$E_{ads} = E_{molec} + E_{slab} - E_{(molec+slab)}, \quad (1)$$

where E_{molec} is the energy of the isolated adsorbate (radical or molecular species) in its equilibrium position, E_{slab} is the total energy of the slab, and $E_{(molec+slab)}$ is the total energy of the adsorbate-slab system. A positive E_{ads} corresponds to a stable adsorbate-slab system. The energy of the isolated adsorbate was determined from calculations performed on a single molecule in a cubic cell with sides of 10 Å. The same Brillouin-zone sampling has been used to calculate the energies of the bare slab and of the molecule-slab systems.

A. Carbon adsorption on the Fe(100) surface

In our previous study related to adsorption and dissociation of CO on the Fe(100) surface, we have also analyzed briefly the adsorption of individual C and O atoms on the Fe(100) surface.[10] In this work, we expand our previous investigations to include in the case of the C atom the coverage effects as well as to analyze the possibility of subsurface absorption. A list of various configurations of the C atom adsorbed on Fe(100) at different surface and subsurface sites is given in Table II together with representative geometric parameters and the corresponding binding energies.

Among various binding sites on the Fe(100) surface adsorption at the hollow $4F$ site was found to be the most stable. The binding energy at this site has a high value of 189.7 kcal/mol at $\theta=0.11$ monolayers (ML). In this configuration, the C atom adsorbs at about 0.4 Å above the surface. The strong bonding of the C atom in this state is due to formation of five bonds with surface Fe atoms, among which four are with atoms in the first layer [$r(Fe^{(I)}\text{-}C)=1.960$ Å] and one with a Fe atom in the second layer [$r(Fe^{(II)}\text{-}C)=1.998$ Å], respectively. The variation of the binding energy of the C atom adsorbed at hollow sites with the increase in coverage over the range (0.11–1.0) is given in Fig. 1 while the corresponding geometric and energetic parameters are provided in Table II. The data presented in Fig. 1 indicates that overall the binding energy decreases with the increase in coverage excepting at 0.5 ML coverage when a slight increase in the binding energy takes place. At $\theta=0.50$ ML, two possible configurations have been analyzed. The first one, indicated as $4F(2)$(close) in Table II, corresponds to the case when two C atoms are positioned at a short separation approximate equal to surface lattice constant, $a_0=2.865$ Å. The second configuration, denoted as $4F(2)c(2\times2)$, corresponds to a $c(2\times2)$ pattern in which the C–C separation is about $a_0\sqrt{2}=4.052$ Å. Among these two configurations, we found that the $4F(2)c(2\times2)$ structure is energetically the preferred one and its binding energy is the one used in Fig. 1 for the case of 0.5 ML coverage.

These findings are also consistent with previous experimental[41] and recent theoretical DFT-PAW results.[17] In particular, based on low-energy electron diffraction (LEED) analysis, it was probed that upon C segregation on the Fe(100) surface, a long-range $c(2\times2)$ ordered structure is formed with the adatoms residing at fourfold hollow sites of

TABLE II. Calculated equilibrium distances (in Å) and adsorption energies (in kcal/mol) for C atoms adsorbed on the Fe(100) surface. The nature of specific adsorption sites as a local minimum on the potential energy surface is also indicated by the corresponding number of imaginary frequencies (N_{imag}).

Configuration	θ	N_{imag}	$r(Fe^{I}\text{-}C)^{a}$	$r(Fe^{II}\text{-}C)$	h(H-surf)[b]	E_{ads}
On surface C adsorption						
$1F(1)$	0.25	2	1.605		1.605	118.3
$2F(1)$	0.25	0	1.755		1.105	154.4
$4F(1)$	0.25	0	1.968	1.958	0.397	186.3
$4F(1)$	0.11		1.960	1.998	0.428	189.7
$4F(2)c(2\times2)$	0.50		2.071	1.865	0.277	187.2
$4F(2)$ (close)	0.50	0	1.953	1.923	0.292	186.0
$4F(3)$	0.75		2.040	1.868		183.4
$4F(4)$	1.00	0	2.031	1.833	0.129	174.0
$4F(4)$-$1F(1)$	1.25	0				158.6
$4F(4)$-$1F(2)$	1.50					148.8
$4F(4)$-$1F(4)$	2.00	0				134.3
$4F(4)$-$2F(1)$	1.25	0				172.8
$4F(4)$-$2F(2)$	1.50					168.3
$4F(4)$-$2F(4)$	2.00	0				164.2
Subsurface C absorption						
$S1(1)$	0.25	0	1.845	1.990–2.132	1.184	161.6
$S1(2)$	0.50		1.838	1.967–2.131	1.301	162.8
$S1(4)$	1.00	0	1.845	2.010–2.035	1.790	157.6
$S2(1)$	0.25	0	1.968	1.729	1.175	153.8
$S3(1)$	0.25			2.038	2.991	152.0

[a]Fe^{I} and Fe^{II} denote iron atoms in the first and second layer, respectively.
[b]This distance is measured perpendicular to the surface.

the substrate. The increased binding energy of C atoms corresponding to $c(2\times2)$ structure relative to the 0.25 ML case has been also observed by Jiang and Carter.[17] These authors have also shown that below 1 ML, the adsorbed carbon atoms are preferred over graphite formation on the Fe(100) surface.

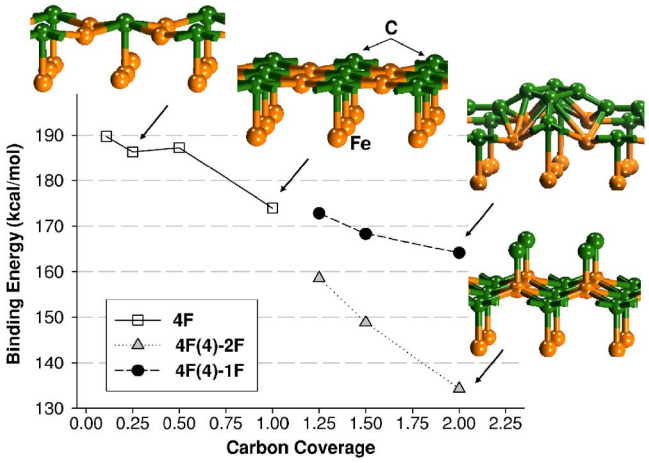

FIG. 1. (Color online) Variation of the binding energy of C atom calculated based on Eq. (1) with respect to surface coverage. Notation mF(n) with $m=1,2,4$ and $n=1,2,4$ refers to adsorption at sites of type m (m=onefold, twofold, and fourfold, respectively) while the index n denotes how many such sites among a maximum of four in the supercell are occupied.

Above 1 ML coverage, adsorption of C atoms on the Fe(100) surface should include mixed types of sites. We assumed that in this case all four hollow sites, denoted $4F(4)$, are occupied and analyze further the occupation of the remaining $1F$ and $2F$ sites. Variation of the binding energies for $4F(4)$-$1F(m)$, $(m=1,2,4)$ and $4F(4)$-$2F(m)$, $(m=1,2,4)$ configurations corresponding to mixed $4F$-$1F$ and $4F$-$2F$ sites is provided in Fig. 1 while the corresponding energy values are given in Table II. Over the coverage range 1.25–2.00 ML it is found that for both occupation schemes, the binding energies decrease with coverage but there is a clear preference for the mixed $4F$-$2F$ configurations. At the largest coverage of 2 ML investigated in this study, the C binding energy of $4F(4)$-$2F(4)$ configuration is 164.2 kcal/mol, a value which is about 30 kcal/mol higher than the one determined for the $4F(4)$-$1F(4)$ configuration. By inspecting the atomic configurations given in Fig. 1, we note that while in the case of $4F(4)$-$1F(4)$ configuration the C atoms remain well separated, in the case of $4F(4)$-$2F(4)$ configuration the C–C covalent bonds between $2F$-$2F$ and $2F$-$4F$ atoms are formed leading to an increased stabilization of this configuration relative to the former one. As a result of C–C interatomic bonding, the Fe surface becomes practically covered by a carbon layer. Such a carbon layer will significantly hinder direct interaction of Fe surface atoms with various gaseous systems that might adsorb on the surface. Further increase in C coverage beyond the 2 ML coverage considered here is expected to lead to graphitic multilayer island formation as was observed experimentally.[42]

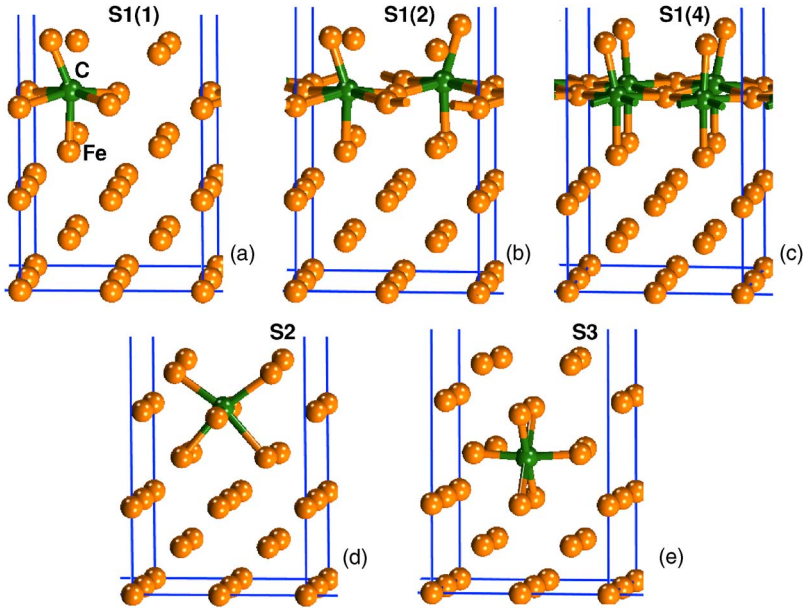

FIG. 2. (Color online) Subsurface absorption configurations of C atom on the Fe(100) surface. Panels (a)–(c) correspond to subsurface site *S*1 at coverages of 0.25 (a), 0.5 (b), and 1.0 (c), respectively. Panel (d) illustrates subsurface site *S*2 while panel (e) corresponds to an octahedral absorption configuration in the second layer, *S*3.

B. Subsurface carbon absorption on Fe(100) surface

In addition to C atom adsorption on the Fe(100) surface, we have also investigated the absorption in subsurface layers. These investigations have been done using a six-layer slab where the top three layers have been allowed to relax. A pictorial view of the resulting equilibrium configurations are given in Fig. 2 and the corresponding geometric and energetic parameters are summarized in Table II.

In the first subsurface layer, we have identified two different adsorption configurations denoted *S*1 and *S*2, which are represented in Figs. 2(a) and 2(d), respectively. In the case of configuration *S*1(1) (the number in parentheses indicates the total number of C atoms in the supercell), the C atom is bonded in a deformed octahedral-like configuration, positioned beneath the 1*F* surface configuration. In this state, the C atom is positioned about 1.18 Å under the top layer and 0.23 Å above the first subsurface layer. It can be noticed that the top Fe atom above the C atom is pushed both upward and laterally relative to its original unperturbed position to accommodate the absorbed C atom. Also, there are significant vertical displacements of the slab layers. For example, the interlayer distances d_{12} and d_{23} between successive slab layers are expanded toward vacuum by 43% and 30% relative to isolated surface, while the d_{34} distance is compressed by 32%. The corresponding bond distances of the subsurface C atom and the neighbor lattice atoms are $r(\mathrm{Fe^{I}}\text{–C})=1.845$ Å with the Fe atom in the top layer, between 1.946 and 2.132 Å with the Fe atoms in the second layer, and $r(\mathrm{Fe^{III}}\text{-C})=1.893$ Å with Fe atom in the third layer. Relative to isolated Fe slab and isolated C atom, the binding energy at subsurface *S*1 site is 161.6 kcal/mol at 0.25 ML coverage, corresponding to an exothermal absorption. By the increase of subsurface coverage to 0.50 ML [see configuration *S*1(2) in Fig. 2(b)] there is a slight increase in the binding energy to 162.8 kcal/mol followed by a decrease to 157.6 kcal/mol at 1.0 ML [see configuration *S*1(4) in Fig. 2(c)]. In this last case, the interlayer distance between the first and second layers (d_{12}), respectively, the second and third layers (d_{23}) increase by 29% and 31%, respectively, relative to the bulk optimized values while a small contraction of −3% is observed for the d_{34} interlayer distance.

The second subsurface configuration identified in this study, denoted *S*2, is also of octahedral type [see Fig. 2(d)] and is positioned beneath the 2*F* surface site. In this case the C atom is bonded to neighbor lattice atoms at distances of 1.968, 1.729, and 2.172 Å, corresponding to iron atoms in the first, second, and third layers, respectively. The interlayer surface relaxations in this case were found quite different from those obtained for the *S*1 site with a compression by −4.7% for d_{12} and an expansion by 3% for d_{34} while the interlayer distance d_{23} is changed little by −0.64%. In this case, however, the largest displacements take place in a horizontal plane along the direction of the Fe atoms in the second layer to which the C atom is bonded. The separation between these Fe atoms is found to be 3.463 Å which represents a 20.8% increase relative to separation of 2.865 Å found in the absence of the C atom. The absorption energy at *S*2 configuration is found to be 153.8 kcal/mol, which is significantly smaller than the value determined for the *S*1 site. Finally, for an even deeper configuration positioned in the third layer, we found a small variation of the corresponding binding energy relative to the *S*2 structure, with a value of 152 kcal/mol.

The absorption of the C atom in the subsurface of Fe(100) has been also analyzed recently by Jiang and Carter[17] using PAW-PBE calculations. These authors have identified only the octahedral subsurface sites similar to the *S*2 type reported here. For this configuration, our calculated absorption energy of 153.8 kcal/mol agrees well with their value of 155.8 kcal/mol at 0.25 ML. However, as we showed above, an even more stable configuration, corresponding to subsurface sites of the *S*1 type can be found with an absorption energy of 161.6 kcal/mol. We note that we have evaluated the vibrational frequencies of the C atom adsorbed at the *S*1 and *S*2 sites (see Table VII in the Appendix) in the frozen phonon approximation, and in all these cases, the vibrational

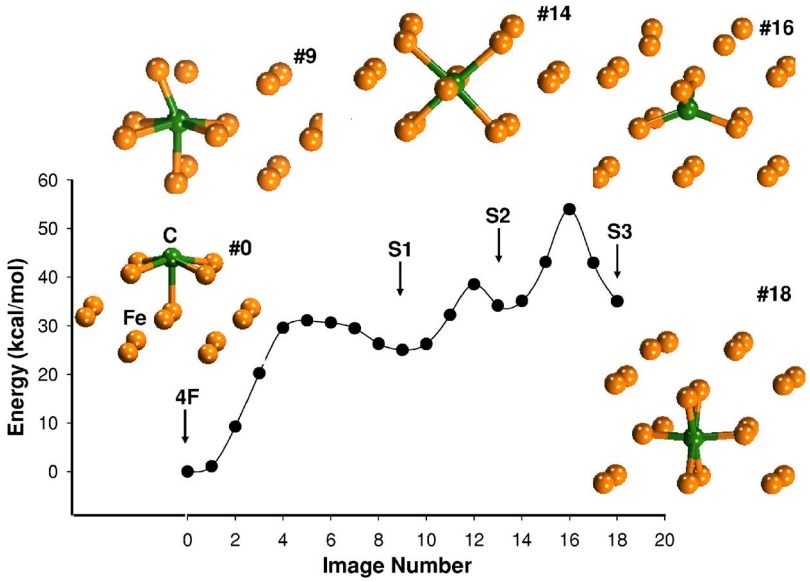

FIG. 3. (Color online) Potential energy surface for C diffusion from a fourfold site to the subsurface $S1$ site followed by diffusion to $S2$ site within the same layer and further to the site $S3$ positioned in the second sublayer. The atomic configurations corresponding to various images along the diffusion pathway are also indicated.

frequencies were positive numbers indicating the existence of stable local minima on the potential energy surface.

C. Surface to subsurface carbon diffusion

In previous sections, we showed that the most stable adsorption configuration of C on the Fe(100) surface is the hollow ($4F$) site while absorption at subsurface sites can take place at both $S1$ and $S2$ octahedral sites. In this section, we analyze the minimum energy pathway for diffusion from a surface $4F$ site to subsurface sites. For this purpose, we have analyzed two different pathways. The first one corresponds to diffusion from the surface $4F$ to the $S1$ subsurface site followed by diffusion to subsurface $S2$ and $S3$ sites. The second pathway represents diffusion from the surface $4F$ site directly to subsurface $S2$ site. Both these pathways have been calculated using the NEB method in connection with a slab model with six layers in which the top three layers were allowed to relax.

The potential energy diagram for the first pathway is given in Fig. 3. We found that diffusion barriers for $4F \rightarrow S1$, $S1 \rightarrow S2$ and $S2 \rightarrow S3$ steps are 31.1 kcal/mol, 12.3 kcal/mol, and 19.9 kcal/mol, respectively. Along $4F \rightarrow S1$, respectively $S2 \rightarrow S3$ pathways, the atom passes through configurations with a tetrahedral type of bonding (see images 5 and 16, respectively, in Fig. 3). Based on this sequence of successive steps, it follows that the entire process is endothermic and the largest barrier is obtained for the initial step corresponding to diffusion from surface to immediately subsurface $S1$ site. Once the C atom reaches the second layer, further diffusion within the same layer or toward the bulk is possible with much lower activation energies. For the second pathway (not shown) corresponding to direct diffusion from $4F \rightarrow S2$ site, we found a similar endothermic process but with a higher diffusion barrier of 39.6 kcal/mol. These results indicate that the $4F \rightarrow S1$ pathway is preferred for surface to subsurface diffusion. These findings are somewhat different from those reported recently by Jiang and Carter.[17] Based on PAW-PBE calculations, these authors have considered only the $4F \rightarrow S2$ pathway for which a diffusion barrier of 33.9 kcal/mol has been determined. However, no evidence of $S1$-type sites has been reported in their study. We noted above the decrease of diffusion barriers once the C atom penetrates to subsurface. Specifically, our barrier of 19.9 kcal/mol corresponding to diffusion among the second and third sublayers (see the $S2 \rightarrow S3$ step) resembles well the diffusion barrier of 19.8 kcal/mol determined by Jiang and Carter for bulk bcc Fe.[43]

The overall picture emerging from these calculations is that the largest barrier for C diffusion from top of the surface toward the bulk is seen for the initial step corresponding to surface to subsurface penetration. Deeper in the bulk, the corresponding diffusion barriers decrease in magnitude to values close to those obtained in bulk.

D. Adsorption and diffusion barriers of CH_x ($x=1,4$) species on the Fe(100) surface

We present in Table III representative geometric and energetic parameters for CH_x species adsorbed at different sites on the Fe(100) surface while the corresponding configurations are depicted in Fig. 4.

1. CH adsorption and diffusion properties

In the case of methylidyne, we analyzed the adsorption configurations on top ($1F$) of the Fe atoms, in a bridge twofold ($2F$) configuration as well as the adsorption at the fourfold hollow site ($4F$) [see panels (a)–(c) in Fig. 4]. The corresponding binding energies given in Table III(a) indicate that there are significant differences in terms of the adsorption energies among these sites with a clear preference for the adsorption at the $4F$ site. At the hollow site, the binding energy relative to isolated CH and the bare surface is 158.2 kcal/mol at $\theta=0.25$ coverage. In this configuration, the CH radical is bonded to four neighbor Fe atoms in the first surface layer with a bond distance $r(\mathrm{Fe^I}\text{-}\mathrm{C})=2.075$ Å, as well as to the lattice atom underneath in the second layer

TABLE III. Calculated equilibrium distances (in Å) and adsorption energies (in kcal/mol) for CH_x ($x=1,4$) species adsorbed on the Fe(100) surface. For selective configurations, we also indicate the number of imaginary frequencies (N_{imag}) of the adsorbate at the respective sites.

Configuration	θ	N_{imag}	$r(Fe^{I}\text{-}C)$[a]	$r(Fe^{II}\text{-}C)$	r(C-H)	θ(H-C-H)	E_{ads}
(a) CH Adsorption							
1*F*	0.25	0	1.643		1.095		110.6
2*F*	0.25	1	1.810	2.251	1.113		125.0
4*F*	0.25	0	2.075	2.076	1.109		158.2
4*F*	0.11		2.049	2.092	1.110		159.7
(b) CH_2 Adsorption							
1*F*	0.25	1	1.803		1.097	112.4	71.9
2*F* (pl)[b]	0.25	1	1.940		1.111	106.8	78.6
2*F*(pp)	0.25	0	1.971		1.102	110.9	86.5
4*F*	0.25	0	2.174	2.145	1.134	101.3	99.6
4*F*	0.11		2.165	2.146	1.134	102.3	101.5
(c) CH_3 Adsorption							
1*F*	0.25	1	2.015		1.099	109.0	32.7
2*F* (pp)	0.25	0	2.174, 2.190		1.109, 1.110, 1.096	108.1, 107.7, 103.1	43.7
2*F* (pl)	0.25	0	2.118, 2.264		1.101, 1.102 1.116	104.4, 104.9 109.0	43.7
2*F* (pp)	0.11		2.178, 2.189		1.108, 1.108 1.097	107.7, 107.4, 103.5	45.5
2*F* (pl)	0.11		2.110, 2.267		1.100, 1.101 1.119	104.5, 104.4 109.0	45.8
(d) CH_4 Adsorption							
1*F* (1 H dn)[c]	0.25		3.611		1.100		0.6
1*F* (2 H dn)	0.25		3.303		1.097		0.4
1*F* (3 H dn)	0.25		3.658		1.094		0.8
1*F* (3 H dn)	0.11		3.658		1.094		0.8
2*F* (1 H dn)	0.25		2.876		1.108		0.9
2*F* (2 H dn)	0.25		4.022		1.096		0.8
2*F* (3 H dn)	0.25		3.220		1.088		0.9
4*F* (1 H dn)	0.25		4.396		1.094		0.9
4*F* (2 H dn)	0.25		4.284		1.094		0.8
4*F* (3 H dn)	0.25		4.146		1.094		0.6

[a]Fe^{I} and Fe^{II} denote iron atoms in the first and second layer, respectively.

[b]The acronyms (pl) and (pp) used here denote a parallel and perpendicular orientation, respectively, of the CH_2 plane relative to the Fe-Fe bond of the lattice atoms involved in bonding.

[c]Notation (m H dn) with $m=1,2,3$ indicates the number of H atoms in CH_4 molecule pointing down to the surface.

with a bond distance $r(Fe^{II}\text{-}C)=2.076$ Å. Upon adsorption, the C-H bond is slightly compressed by 0.25 Å relative to the gas phase value. By decreasing the coverage to an even lower value of 0.11 ML, the binding energy increases slightly to 159.7 kcal/mol.

The compression of the C-H bond upon adsorption on the surface is expected to lead to a blue shift of the corresponding stretching mode. Based on the vibrational frequency analysis in the frozen phonon approximation, we determined that this is indeed the case. Specifically, the stretching frequency of the adsorbed CH species at the hollow site was found to be 2919 cm^{-1}. This value is 145 cm^{-1} larger than the corresponding calculated gas phase frequency. This upshift of the adsorbed CH on Fe(100) is consistent to experimental observations. Indeed, Hung and Bernasek[44] have determined based on high-resolution electron-energy-loss spectroscopy (HREELS) measurements, a vibrational frequency of 3010 cm^{-1} for the adsorbed CH on Fe(100), corresponding to a blueshift of 152 cm^{-1} relative to the experimental gas phase value. This value is closely matched by our predicted blueshift value.

Beside the hollow 4*F* site, the on-top 1*F* site was also found to correspond to a local minimum (see Table VII) while the vertical 2*F* bridge configuration was found to correspond to a transition state. For the transition state at the 2*F* site, the eigenvector corresponding to the imaginary frequency identified was found to be a frustrated translation pointing to the 4*F* hollow site. Consequently, it can be con-

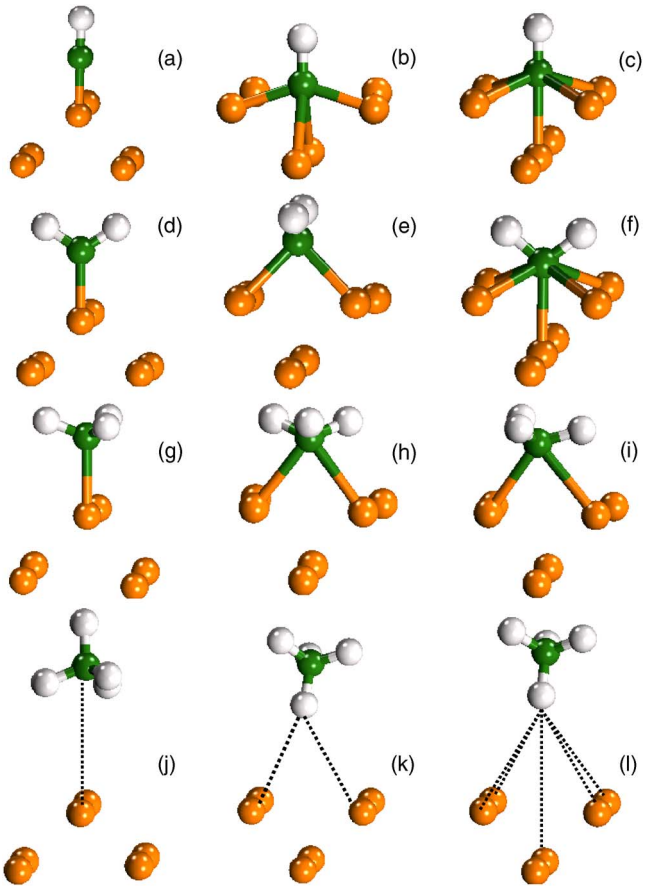

FIG. 4. (Color online) Representative adsorption configurations of CH_x ($x=1,4$) species on Fe(100) surface. Panels (a)–(c) correspond to the CH species adsorbed at (a) onefold (on top), (b) twofold (bridge), and (c) fourfold hollow sites. Panels (d)–(f) illustrate CH_2 adsorption at (d) onefold, (e) twofold perpendicular, $CH_2[2F(pp)]$, and (f) fourfold surface sites. Panels (g)–(i) indicate adsorption configurations of CH_3 at (g) onefold and (h), (i) twofold sites. In these last two cases both the perpendicular, $CH_3[2F(pp)]$, and the parallel, $CH_3[2F(pl)]$, structures described in text are represented. Panels (j)–(l) present representative adsorption configurations of CH_4 adsorbed at (j) $1F$, CH_4 $(1F,3dn)$, (k) $2F$, CH_4 $(2F,1dn)$, and (l) $4F$, CH_4 $(4F,1dn)$ sites, respectively.

cluded that the minimum energy path for CH diffusion among neighbor $4F$ sites has a transition state at the $2F$ site and the corresponding diffusion barrier is 33.2 kcal/mol.

2. CH_2 adsorption and diffusion properties

In the case of methylene, adsorption at $1F$, $2F$, and $4F$ sites has been considered [see configurations (d)–(g) in Fig. 4]. The results given in Table III(b) indicate that adsorption at the hollow site is the most stable with a binding energy of 99.6 kcal/mol at $\theta=0.25$ ML coverage, respectively 101.5 kcal/mol at $\theta=0.11$ ML. Similar to CH adsorption, the increased stability at the $4F$ site relative to the other $1F$ and $2F$ sites is due to formation of five Fe-C bonds, four of them with Fe atoms in the first layer (at a distance of about 2.174 Å), and one bond with a Fe atom in the second layer (at a distance of 2.145 Å). In the case of adsorption at the bridge site, we have analyzed two configurations in which the CH_2 plane is parallel [see configuration denoted $2F$(pl) in Fig. 4(e)] and perpendicular [see configuration denoted $2F$(pp) in Fig. 4(f)], respectively, to the Fe-Fe bond underneath. Among these two states, the perpendicular configuration [$2F$(pp)] is the most stable and has a binding energy of 86.5 kcal/mol.

Based on the vibrational frequency analysis in the approximation of a frozen lattice, we have determined that $4F$ and $2F$(pp) states are local minima while the other two states, i.e., $2F$(pl) and $1F$, represent transition states on the potential energy surface. Specifically, in the case of the most stable $4F$ configuration, there are significant downward shifts of the C-H vibrational frequencies with values of 2633 and 2615 cm^{-1} for the asymmetric and respective symmetric stretches and an upward shift to 1212 cm^{-1} for the H-C-H bending mode relative to the gas phase values.

Regarding the diffusion properties of CH_2 molecule on the surface, we have analyzed the minimum energy path for motion among the $2F$(pp) and $4F$ configurations using the NEB method. Our results (not shown) have confirmed the existence of a local minimum at the $2F$(pp) configuration. Additionally, we have determined a small diffusion barrier of only 0.43 kcal/mol when going from $2F(pp)\rightarrow 4F$ sites while the reverse diffusion process $4F\rightarrow 2F(pp)$ has a diffusion barrier of 13.5 kcal/mol. The other possible diffusing pathway of CH_2 molecule among neighbor $2F$(pp) configurations passing through the $1F$ site requires a higher activation energy of 14.6 kcal/mol. In this the transition state is at the $1F$ site, a fact also confirmed by the vibrational analysis (see entry $1F$ corresponding to CH_2 molecule in Table VII).

3. CH_3 adsorption and diffusion properties

In the case of the methyl radical, our calculations indicate that stable adsorption configurations can be determined only for adsorption at the $2F$ site [see Figs. 4(h) and 4(i)]. At this site, two configurations of the CH_3 radical have been analyzed, namely with one of the C-H bonds perpendicular [$2F$(pp), see Fig. 4(h)] respectively parallel [$2F$(pl), see Fig. 4(i)] to the Fe-Fe surface direction. It was obtained [see Table III(c)] that both these configurations have similar binding energies of about 43.7 kcal/mol at $\theta=0.25$ coverage. By decreasing the coverage to 0.11 ML, the binding energy increases slightly to 45.8 kcal/mol for $2F$(pp) and 45.5 kcal/mol for $2F$(pl) states, respectively. As a result of adsorption the C-H bond distances are elongated by as much as 0.036 Å (at 0.25 coverage) relative to the gas phase structure while softening of the C-H stretching modes takes place (see Table VII). We note that both $2F$(pp) and $2F$(pl) adsorption configurations are local minima as has been confirmed based on vibrational frequency analysis. In contradistinction, for the $1F$ configuration [see Fig. 4(g)], we have obtained one imaginary frequency indicating that this state corresponds to a transition state. The eigenvector corresponding to this imaginary frequency indicates a frustrated translation pointing from the $1F$ site to the neighbor $2F$ site. Consequently, the diffusion pathway of CH_3 radical among two $2F$ sites has a transition state at $1F$ site and a corresponding diffusion barrier of 4.0 kcal/mol.

TABLE IV. Calculated equilibrium distances (in Å) and adsorption energies (in kcal/mol) for CH_x ($x=1,4$), C, H, O, and CO species adsorbed at the most stable sites on the Fe(100) surface based on PAW-PBE calculations.

Configuration	θ	$r(Fe^{I}\text{-}X)$[a]	$r(Fe^{II}\text{-}X$[b])	r(C-H)	θ(H-C-H)	r(C-O)	E_{ads}^{PBE}
H (4*F*)	0.25	2.075	1.739				60.7
	0.11	2.043	1.797				61.1
C (4*F*)	1.00	2.008	1.828				176.3
	0.50	2.026	1.894				191.6
	0.25	1.949	1.969				190.3
	0.11	1.942	1.981				193.2
CH (4*F*)	0.25	2.041	2.067	1.113			161.3
	0.11	2.032	2.104	1.116			163.2
CH_2 (4*F*)	0.25	2.174	2.107	1.139	101.4		100.5
	0.11	2.144	2.135	1.142	102.4		101.8
CH_3 (2*F*)	0.25	2.161		1.100	107.9		43.0
		2.131		1.114	103.2		
	0.11	2.177		1.099	108.0		43.9
				1.112	103.6		
CH_4 (1*F*)	0.25	3.673		1.097	109.4		0.5
	0.11	3.643		1.098	109.4		0.4
O (4*F*)	0.25	2.096	2.122				147.1
	0.11	2.051	2.166				148.6
CO (4*F*)	0.25	1.955	2.080			1.320	48.9
		2.227					
	0.11	1.955	2.136			1.318	49.1
		2.183					

[a] Fe^{I} and Fe^{II} denote iron atoms in the first and second layer, respectively.

[b] *X* stands for C in the case of C, CH, CH_2, CH_3, CH_4, and CO adsorption, and for H in the case of H adsorption, respectively.

4. CH_4 adsorption properties

In the case of methane molecule, we have analyzed the dependence of the adsorption energy both as a function of the surface site (1*F*, 2*F*, and 4*F*) as well as for several orientations of the molecule relative to the surface, namely with one, two, and three H atoms, respectively, oriented toward the surface. As indicated in Table III(d), our results show that over the entire range of molecular orientations and surface sites considered, the CH_4 molecule adsorbs very weakly on the Fe(100) with values between 0.4 and 0.9 kcal/mol. We notice that there is a slight preference for adsorption of CH_4 molecule above a surface Fe atom, in a configuration with three of the H atoms pointing to the surface, hereafter denoted as 1*F*(3dn) configuration, and above a hollow site in a configuration with one H atom pointing to the surface, hereafter called 4*F*(1dn) configuration. Independent of the adsorbed state, the molecule is positioned at large distances from the surface with Fe-C separations in the range 3.3–4.3 Å. These results indicate that CH_4 molecule is only weakly physisorbed on the Fe surface. We need to emphasize however that the weakly bounded molecular states described above should be considered carefully as current implementations of DFT do not have the right physics to account for van der Waals interactions and consequently might not provide an accurate description of such weakly bound states. Due to these limitations, we have not attempted further characterization of these states.

E. Comparison of USPP and PAW results

The results presented in previous sections have been obtained using ultrasoft pseudopotentials in connection with the PW91 exchange-correlation functional. As was indicated in the computational section, we have also checked the accuracy of these results against the PAW-PBE method.

We provide in Table IV the results of PAW calculations for the adsorption energies of CH_x ($x=0,4$) species on the Fe(100) surface. In this case only the most stable adsorption configurations as determined from USPP method have been considered. By comparing the USPP-PW91 and PAW-PBE results, we observe very small differences among these two sets of values for the case of CH (1.97%), CH_2 (0.88%), and CH_3 (−1.46%) species. In the case of C adsorption, the PAW-PBE result is slightly larger than USPP value by 2.1%, respectively. The largest variation is found, however, in the binding of the CH_4 molecule for which the PAW-PBE result is about 0.5 kcal/mol. We further tested the binding of this state using the PAW-PW91 method and found a binding energy of 0.9 kcal/mol, which is basically the same result as obtained using the USPP-PW91 method. As we noticed before, this configuration corresponds however to a physisorbed state and, as a result, the current implementation of DFT might not be very accurate for describing this state. Overall, the comparison of USPP-PW91 to PAW-PBE sets of results indicates that the calculated binding energies at these

levels of theory are close to each other within a 3.9% interval. We are not aware of any accurate experimental data which can be used to compare and differentiate among the results of these calculations. In the case of C adsorption at the 4*F* hollow site, an adsorption energy of 190.0 kcal/mol at 0.25 ML has been determined recently by Jiang and Carter based on PAW-PBE method.[17] This result is very close to the value of 190.3 kcal/mol that we have determined in this study at PAW-PBE level of theory.

In the case of the C atom, we have extended the set of calculations to further characterize the adsorption at the bridge 2*F* site. Based on USPP-PW91 calculations, the nature of this state is not very clear as there is a shallow potential in the region of the 2*F* state followed by a rapid decrease once the C atom moves toward the 4*F* site. Based on PAW-PBE calculations, we determined that vibrational frequencies of the C atom adsorbed at the 2*F* site are 863.5, 263.5, and 92.8*i* cm^{-1}. The first two vibrational frequencies are very close to those obtained using USPP-PW91 method (see Table VII) but the third imaginary frequency indicates that this configuration is a transition state for diffusion of the C atom among the hollow sites. The barrier height for this diffusion pathway is calculated to be 30.8 kcal/mol at the PAW-PBE level, a value which is similar to the USPP-PW91 result of 31.9 kcal/mol.

As will become evident in the next section, adsorption of individual H, O, and CO species on Fe(100) will be considered in connection with dissociation reactions of CO followed by successive hydrogenation steps. For consistency with the results reported for CH_x species, we expand our discussion here to include the binding energies for H, O, and CO species calculated using the PAW-PBE method. This comparison is necessary as our previous calculations[10] were done only using the USPP-PW91 method. The results reported in Table IV for H, O, and CO species were considered only for the case of adsorption at the hollow 4*F* site. As was shown before,[10,15] the hollow site corresponds to the most stable adsorption configuration on the Fe(100) surface for all these species. In the case of H, the corresponding value of 60.7 kcal/mol at PAW-PBE level is practically identical with the USPP-PW91 result of 60.7 kcal/mol we reported earlier.[15] For the O atom, the PAW-PBE result of 147.1 kcal/mol at 0.25 ML is only 1.4% larger than the USPP-PW91 value of 145.0 kcal/mol.[12] Finally, in the case of the CO molecule adsorbed at the hollow site, we found that this adopts a tilted configuration similar to that described in our previous study.[10] The molecule is tilted by 49.3° at PAW-PBE theoretical level with respect to the surface normal while the CO bond is significantly elongated to 1.320 Å, relative to the gas phase value of 1.143 Å, respectively. These sets of values are also very close to the USPP-PW91 predictions which indicate a tilt angle of 48° and a C-O bond length of 1.321 Å. The binding energies at PAW-PBE theoretical level of 48.9 kcal/mol is slightly larger than the USPP result of 46.7 kcal/mol at 0.25 ML.[10]

Overall, the results for binding energies of CH_x ($x=1,4$), H, O, and CO species presented in this section indicate that the USPP-PW91 data follow closely the results obtained using the PAW-PBE method.

TABLE V. Calculated average magnetic moments (in Bohr magneton units, μ_B) of the iron atoms in the first three layers of the slab as function of coverage as determined based on US-PW91 and PAW-PBE calculations. Adsorption of C atoms at hollow 4*F* and octahedral *S*1 sites has been considered for surface and subsurface analyses, respectively.

Surface Layer[a]	Bare Surface	C Surface Adsorption			C Subsurface Adsorption		
		0.25	0.50	1.0	0.25	0.50	1.0
				(a) US-PW91			
S	3.05	2.72	2.49	2.21	2.88	2.79	2.53
S−1	2.45	2.38	2.15	1.88	2.24	2.23	2.05
S−2	2.56	2.48	2.47	2.49	2.45	2.37	2.20
				(b) PAW-PBE			
S	2.94	2.60	2.31	1.97			
S−1	2.36	2.33	2.10	1.66			
S−2	2.39	2.38	2.25	2.28			

[a]*S*, *S*−1, and *S*−2 denote the surface, first, and second subsurface layers, respectively.

F. Magnetic properties

Given the magnetic nature of bcc iron, it is important to analyze the modification of the magnetic moments as a result of C adsorption both on surface as well as at subsurface sites. For this purpose, we present in Table V the variation of the magnetic moments for the bare Fe slab and for the case when C is adsorbed on the surface at the 4*F* hollow site and the respective subsurface, at the octahedral S1 sites, at different coverages.

By analyzing the variation of the magnetic moments in the top three layers of the bare slab, we notice a significant enhancement of the magnetic moments relative to the bulk value of $2.32\mu_B$ ($2.20\mu_B$) as determined based on US-PW91 (PAW-PBE) calculations. Both these computational levels indicate a similar variation of the magnetic moments with a maximum of $3.05\mu_B$ ($2.94\mu_B$) at the top surface layer. This variation is similar to that determined by Ohnishi *et al.*[45] based on accurate full-potential linearized augmented-plane-wave (FLAPW) calculations.[44] Specifically, these authors have determined values of 2.39 ($S-2$), 2.35 ($S-1$), and $2.98\mu_B$ (S) for the magnetic moments of the top three surface layers of Fe(001), values which are very close to the PAW-PBE results obtained here. The enhancement of the surface magnetism was shown to be due to existence of surface states.[45]

By the increase in coverage of the adsorbed C atoms, we notice from the data presented in Table V that a significant demagnetization of the iron layers takes place. Both the magnetization of the surface (S) and the subsurface ($S-1$) layers is effected while the effect upon the second subsurface layer ($S-2$) is less pronounced. In the case of the ($S-1$) layer, the most important changes are observed for the case of the Fe atom directly bonded to the C atom adsorbed at the 4*F* site. For example, based on PAW-PBE results at $\theta=0.25$ coverage, the magnetic moment of the Fe atom involved in bonding decreases to $1.98\mu_B$ while the other three Fe atoms in the

TABLE VI. Calculated binding energies for H, C, O, CO, and CH_x ($x=1,4$) species as determined from USPP-PW91 calculations in the case of a surface with (a) coadsorbed C atom at hollow site, C($4F$); (b) coadsorbed subsurface C atom at a subsurface $S1$ site; C[$S1(1)$], at 0.25 coverage; (c) coadsorbed subsurface C atoms at $S1$ site, at full coverage, C[$S1(4)$]. The values in parentheses represent the percentage increase of the binding energy of respective species in the coadsorbed cases relative to the case when no C coadsorption is considered.

	H($4F$)	C($4F$)	O($4F$)	CO($4F$)	CH($4F$)	CH_2($4F$)	CH_3($2F$)	CH_4($1F$)
C($4F$)	63.3	188.1	148.6	52.3	164.4	105.6	42.4	0.88
	(5.8%)	(1.0%)	(2.7%)	(11.9%)	(3.9%)	(6.0%)	(−3.0%)	(3.6)
C[$S1(1)$]	62.2	188.9	149.3	48.2	159.0	101.3	54.5	1.98
	(3.9%)	(1.4%)	(3.2%)	(3.4%)	(0.5%)	(1.7%)	(24.7%)	(131.4)
C([$S1(4)$]	60.1	191.6	148.3	51.6	166.6	104.5	55.0	0.9
	(0.5%)	(2.9%)	(2.5%)	(10.7%)	(5.3%)	(5.0%)	(25.8%)	(3.9)

same subsurface layer of the slab have higher magnetic moments of 2.41, 2.46, and $2.46\mu_B$, respectively. Similarly, at $\theta=0.5$ coverage, the Fe atoms in the subsurface layer bonded directly to C have reduced magnetic moments of about $1.66\mu_B$, while the other two free Fe atoms of the same layer have significantly larger magnetic moments of $2.55\mu_B$. We note that the values reported in Table V correspond to the average magnetic moments for specific layers and not to the local site values as detailed above. Focusing now on the magnetic moment of the C atom, we note that this is always antiparallel to the Fe moment with values ranging from $-0.19\mu_B$ to $-0.15\mu_B$ when the C coverage increases from 0.25 to 1.0 ML.

The demagnetization effect observed upon C adsorption on the surface also holds for the case of subsurface adsorption as indicated by the US-PW91 data given in Table V. In this case however it can be observed that by the increase in C coverage at the subsurface $S1$ site, there is a reduction of the magnetic moments not only in the top and subsurface layers but also in the second $(S-2)$ layer.

The quenching of magnetic moments of Fe atoms observed upon C adsorption is also present in the case of the other CH_x ($x=1,3$) adsorbates but its magnitude is dependent on the individual system. For example, based on PAW-PBE calculations, we found that upon adsorption of the CH_x species, the average magnetic moment of the Fe atoms in the first layer is always smaller than the one found for the bare surface with values of $2.64\mu_B$, $2.73\mu_B$, and $2.84\mu_B$ for the case of CH($4F$), CH_2($4F$), and CH_3($2F$) adsorbed species, respectively. A decrease of the magnetic moment also takes place for the atoms in the subsurface layer bonded to the C atom of CH and CH_2 species, respectively.

Overall, the results presented in this section indicate that the C and CH_x ($x=1,3$) species lead to a demagnetization of surface Fe atoms. However, this effect is primarily limited to the atoms directly bonded to the adsorbates. A similar effect has been observed to take place in the case of CO chemisorption on γ-Fe/Cu(100).[46]

G. Coadsorption effects induced by C atom

We have shown in Sec. III A that upon the increase in C coverage from 0.25 to 0.5 ML a preferential $c(2\times2)$ pattern is formed with a corresponding increase in the C atom binding energy. In this section, we analyze whether this coadsorption effect is limited to the case of C atoms or if there is also an additional stabilization effect upon the other H, O, CO, and CH_x ($x=1,4$) adsorbate species. Among various relative positions of the coadsorbed H, O, CO, and CH_x species and the C atom, we limit ourselves to the analysis of a $c(2\times2)$-like pattern which was found to be optimal in the case of C adsorption. Exception from this pattern was considered in the case of CH_3 adsorption where the most stable binding site is the bridge $2F$ configuration and in the case of CH_4 adsorption where we have analyzed the binding above a surface atom site having CH_4 ($1F$, 3dn) configuration. The results of these coadsorption studies at 0.25 ML C coverage are provided in Table VI. In this table, we indicate the binding energies of various atomic and molecular species as a result of C coadsorption, while in parentheses, we present the percentage difference relative to the case when no coadsorption takes place (adsorption on the bare surface). As can be seen from the data in Table VI, for the great majority of cases analyzed, the binding energies of the individual species increase as a result of C coadsorption. In particular, we notice the largest variations in the case of CO and CH_2 species for which the binding energies increase by 11.9% and 6.0%, respectively. The only noticeable exception for this additional stabilization trend was found for the case of C coadsorbing with CH_3. In this case however there is a repulsive interaction between C and CH_3 species due to the small separation of 3.48 Å between these species.

A possible explanation for the increased stability of the adsorbed CO or CH_2 species when C coadsorption is involved is the existence of local strain effects of the surface. In our previous work,[10] we have shown that in the case of the Fe(100) surface, there is a direct proportionality between the binding energy of CO and the lattice expansion at different surface stresses. In the present work, we note that the local surface environment is significantly expanded by the presence of the coadsorbed C atom. For example, we have determined lateral expansions of the Fe-Fe distances as high as 6% for CO ($4F$) and 3.9% for CH_2 ($4F$) relative to adsorbed configurations on the bare surface indicating that the local lattice structure is significantly altered by the coadsorbed C atom.

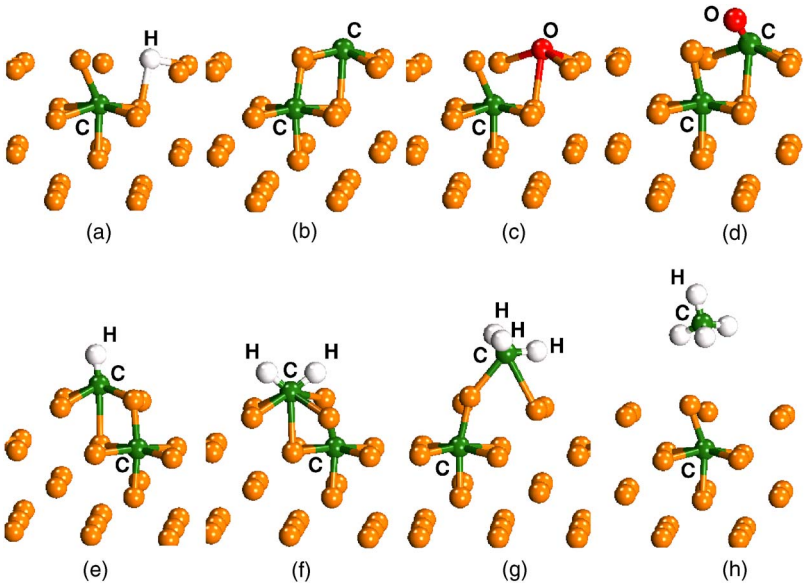

FIG. 5. (Color online) Coadsorption configurations of atomic (H, C, and O) and molecular or radical (CO, CH, CH_2, CH_3, and CH_4) species and a C atom absorbed at a subsurface *S*1 site.

A second category of coadsorption tests were done for the case when the C atom is absorbed at a subsurface *S*1 site. In this case, we analyzed two subsurface C coverages of 0.25 ML and 1 ML, respectively. Selective optimized configurations of different species adsorbed on such a C-treated surface are given in Fig. 5 (for 0.25 ML C) and in Fig. 6 (for 1.0 ML C) while the variations of the binding energies relative to the bare surface case are provided in Table VI {see entries C[*S*1(1)] and C[*S*1(4)]}. It can be seen that in both these two situations, the adsorption energies of various atomic and molecular species analyzed here increase relative to the case when adsorption takes place on the bare surface with the largest variations being observed for CO and CH_3 species. Moreover, for the C-containing species C, CO, CH, CH_2, and CH_3, the increase of subsurface carbon coverage from 0.25 to 1 ML leads to an extra stabilization as illustrated by data in Table VI {see entries C[*S*1(1)] and C[*S*1(4)]} and in Fig. 7(e).

Based on these findings, it can be concluded that the surface with preadsorbed C at surface or subsurface sites leads to an increased stabilization for the adsorbed H, C, O, CO, and CH_x surface species. We also evidenced that the stabilizing effect increases with the increase of subsurface carbon coverage. Based on these findings, it is expected that some important differences in chemisorption properties of the atomic and molecular species will be observed in the case of iron carbide surfaces relative to the situation of iron surface analyzed in this study.

H. Hydrogenation reactions of CH_x species

Having determined the relative stabilities of various CH_x (x=0,4) species, we are focusing now on the analysis of the minimum energy paths for successive hydrogenation reactions of CH_x species leading to formation of CH_4 on the Fe(100) surface. These investigations have been done using the NEB method of Jónsson and Mills.[37]

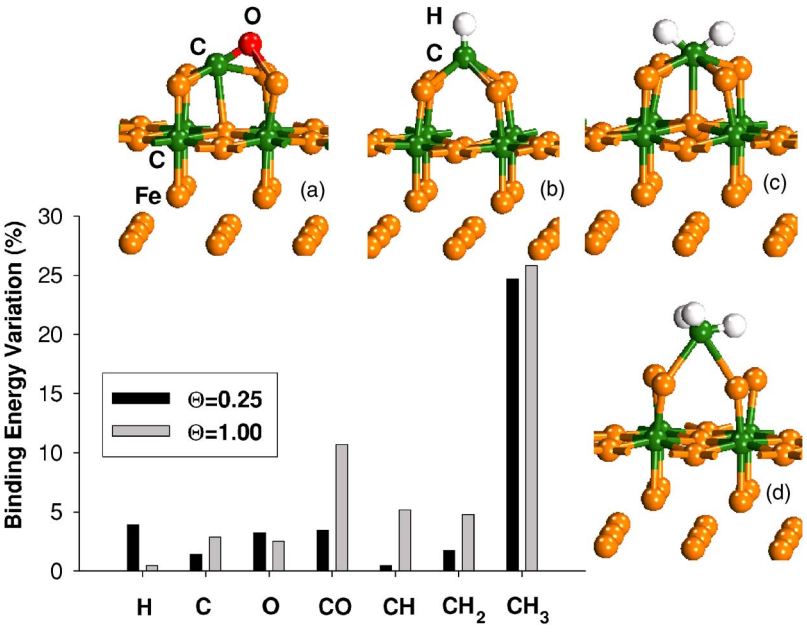

FIG. 6. (Color online) Adsorption configurations of (a) CO, (b) CH, (c) CH_2, and (d) CH_3 species on Fe(100) surface with subsurface C atoms absorbed at *S*1 sites at full coverage. Panel (e) indicates the variation of the binding energies for specific atomic and molecular species for different coverages of C atoms absorbed at subsurface *S*1 sites.

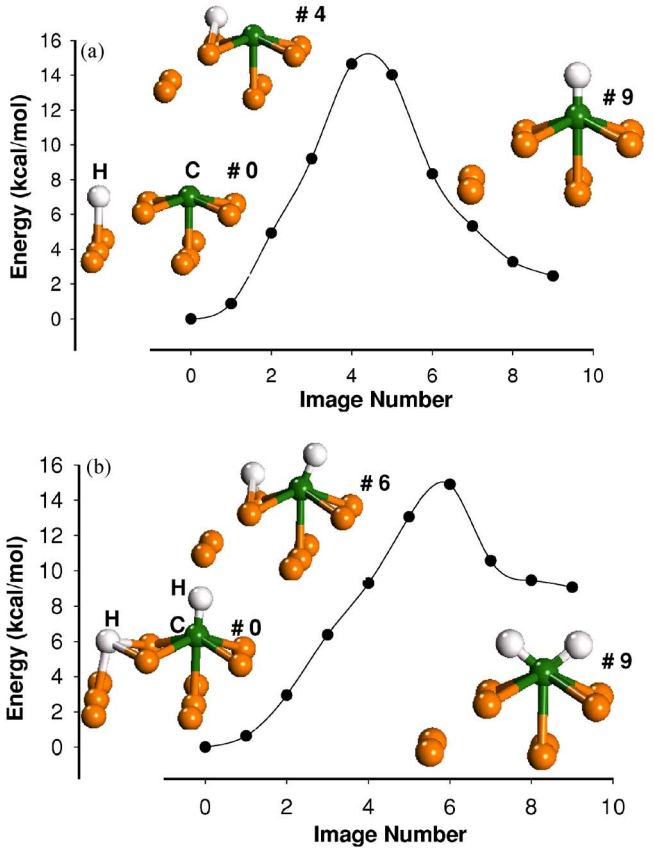

FIG. 7. (Color online) Potential energy surface for hydrogenation reactions: (a) $H(4F)+C(4F)\rightarrow CH(4F)$; (b) $H(4F)+CH(4F)\rightarrow CH_2(4F)$.

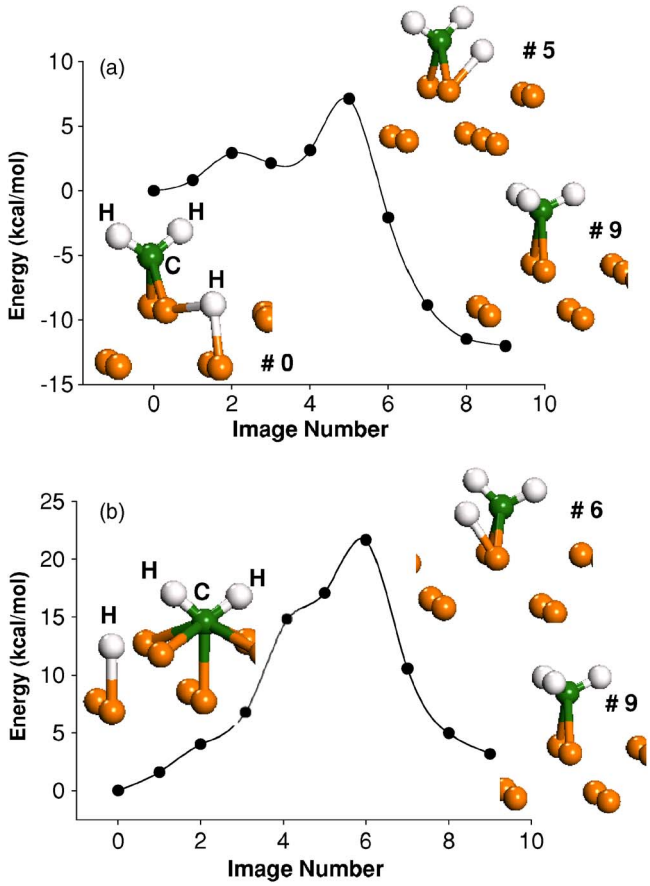

FIG. 8. (Color online) Potential energy surface for hydrogenation reactions: (a) $H(4F)+CH_2(2F)\rightarrow CH_3(2F)$; (b) $H(4F)+CH_2(4F)\rightarrow CH_3(2F)$.

The first hydrogenation step corresponds to reaction $H(4F)+C(4F)\rightarrow CH(4F)$. In this case, we considered as starting and ending states the most stable adsorption configurations for both the reactants and the product. As indicated in this study, these states correspond to adsorption at the hollow sites. The minimum energy path for methylidyne formation as calculated using the USPP-PW91 method is given in Fig. 7(a). In this process, a H atom, initially positioned at a $4F$ site, diffuses through the bridge configuration and reacts with a C atom adsorbed at the neighbor hollow site, leading ultimately to formation of a CH species. The corresponding barrier height of this process is about 14.6 kcal/mol. This hydrogen step has been also analyzed using the PAW-PBE method using the adsorption configurations optimized at this level of theory. Our results indicate that in this case the barrier height increases slightly to 16.6 kcal/mol relative to the USPP-PW91 result.

The reaction path for the second hydrogentation step, $H(4F)+CH(4F)\rightarrow CH_2(4F)$, is given in Fig. 7(b). This corresponds to hydrogenation of methylidyne and formation of methylene. The reaction profile has a barrier similar to the one found in the first hydrogenation step of 14.9 kcal/mol. In this process, the H atom initially positioned at a hollow site passes through a bridge configuration and moves to the hollow site where the CH species is adsorbed. For the same reaction step leading to methylene formation, the results of NEB calculations based on the PAW-PBE method give a barrier of 16.3 kcal/mol, similar to that determined for the first hydrogenation step of 16.6 kcal/mol. Overall we found that independent of the computational method used, i.e., USPP-PW91 or PAW-PBE, both the first and the second hydrogenation steps are endothermal processes with similar activation energies.

The hydrogenation step leading to formation of CH_3 is detailed in Fig. 8 for the case of the USPP-PW91 results. In this case, we analyzed two reaction profiles corresponding to two different initial states. The first one corresponds to $CH_2(2F)+H(4F)\rightarrow CH_3(2F)$ [see Fig. 8(a)] while the second one to $CH_2(4F)+H(4F)\rightarrow CH_3(2F)$ [see Fig. 8(b)]. As indicated in Fig. 8(a), in the first process, there are two barriers of 2.9 kcal/mol and 7.1 kcal/mol, respectively, separated by a small local minimum. This intermediate minimum corresponds to a configuration $CH_2(2F)+H(2F)$ [image 4 in Fig. 8(a)] in which both the CH_2 and H species are adsorbed at bridge sites. A similar minimum energy path profile is obtained in the case of PAW-PBE calculations with corresponding barriers of 3.2 kcal/mol and 6.0 kcal/mol, respectively.

If we consider however as the initial state, the case where both CH_2 and H species are adsorbed at their most stable configurations, namely $4F$ sites, the minimum USPP-PW91 energy profile is different as can be seen in Fig. 8(b). In particular, in this case, the barrier height is significantly in-

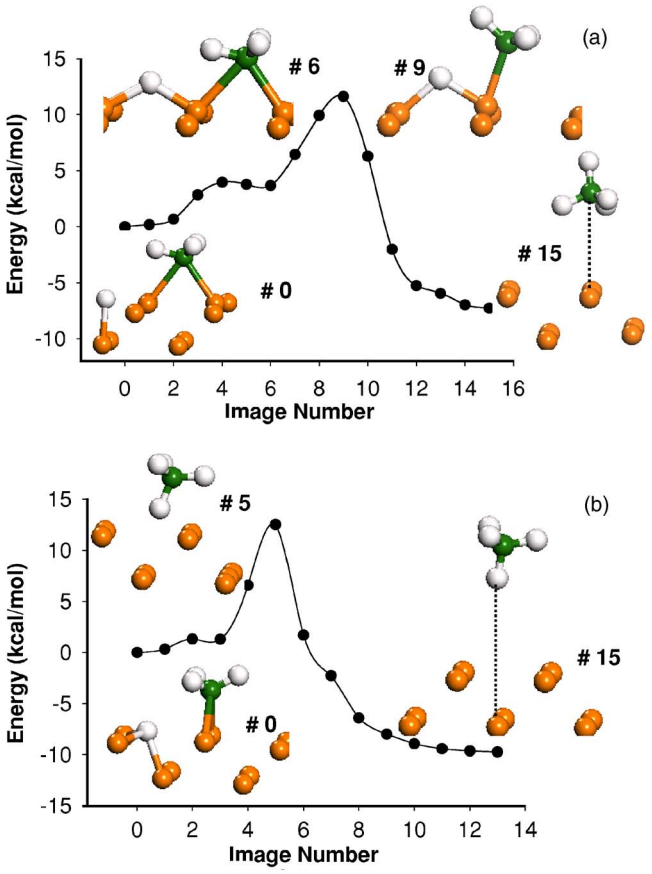

FIG. 9. (Color online) Potential energy surface for hydrogenation reactions: (a) $H(4F)+CH_3(2F)\rightarrow CH_4(1F)$; (b) $H(4F)+CH_3(2F)\rightarrow CH_4(4F)$.

creased to about 19.8 kcal/mol while reaction is overall endothermal. For this last reaction step, the barrier obtained using PAW-PBE method is 18.8 kcal/mol.

In Fig. 9, we illustrate the reaction profile corresponding to hydrogenation reaction of CH_3 radical leading to CH_4 formation. In the initial state, the H atom is adsorbed at the hollow state while methyl radical is adsorbed at a bridge site. In the initial stage (see images 0–6 in Fig. 9(a)) the H atom moves from the $4F$ sites to a $2F$ site placed laterally from the adsorbed CH_3. This process requires overcoming a small barrier of about 4 kcal/mol. From this configuration the H and CH_3 can react directly after an additional barrier of about 8 kcal/mol is surpassed, leading to formation of CH_4 above a surface Fe atom in the $CH_4(1F, 3dn)$ configuration. Overall, the barrier of this entire hydrogenation step is equal to 11.6 kcal/mol while the reaction is exothermal.

The above pathway corresponds to the case when the impinging H atom is attaching to the adsorbed CH_3 following a pathway through a bridge configuration positioned laterally [see image 6 in Fig. 9(a)] relative to the site where CH_3 is initially adsorbed. Beside this pathway, we have also considered a second case in which the impinging H atom comes directly from the hollow site toward the adsorbed CH_3 species adsorbed initially at a bridge site [see Fig. 9(b)]. The overall activation energy of this process is slightly larger than the process analyzed in Fig. 9(a) with a value of 12.5 kcal/mol. However, the reactions described by both these two pathways are exothermal in nature.

I. Potential energy diagram for CO and H_2 dissociation and hydrogenation of CH_x ($x=0,3$) species on the Fe(100) surface

The results obtained in the previous sections related to stability and hydrogenation reactions of CH_x ($x=1,4$) species on the Fe(100) surface can be further correlated to our previous results on adsorption and dissociation properties of CO and H_2 systems on the same iron surface.[10,15] In this section, we are particularly interested to determine the potential energy diagram for the early elementary surface steps that might be involved in the Fischer-Tropsch process on the Fe surface.

We have shown in Ref. 15 that dissociative chemisorption of H_2 can take place with a small activation energy of about 2 kcal/mol, a result that is in agreement with experimental findings of Burke and Madix.[7] In the CO case, experimental work done in Bernasek group[4] has demonstrated that adsorption takes place predominantly at the hollow site (at the so-called α_3 state). From this state, the CO molecule can further dissociate, i.e., $CO(4F)\rightarrow C(4F)+O(4F)$, leading to formation of adsorbed C and O species at neighbor hollow sites. In our previous study,[10] we have demonstrated that adsorption at the hollow site corresponds indeed to the most stable configuration and a barrier height of 24.5 kcal/mol has been determined for dissociation of CO with formation of C and O adsorbed species. As this activation energy was found to be smaller than the calculated binding energy of CO in the α_3 state of 46.7 kcal/mol, it follows that dissociation precludes the desorption process, in agreement with the model proposed by Cameron and Dwyer.[47] As a result of the H_2 and CO dissociation steps described above, the iron surface will be initially decorated with C, O, and H atoms species adsorbed predominantly at hollow sites. We have also shown in our previous study[15] that diffusion barrier of the H atom on the Fe(100) surface is very small, with values of about 1.22 kcal/mol. Consequently, the H atoms can easily diffuse on the surface and further participate in reactions with adsorbed C or O species.

In this study, we focus only on the hydrogenation reactions of the adsorbed C atoms through the sequence $C\rightarrow CH\rightarrow CH_2\rightarrow CH_3\rightarrow CH_4$ leading ultimately to methane formation. It is important to note that besides this set of reactions analyzed here, other reactions such as those between adsorbed H and adsorbed CO or O species are also possible. However, this last category of reactions will not be addressed in the current study.

The energetic diagram corresponding to adsorption and dissociation of H_2 and CO molecules and to sequential hydrogenation of C to CH_4 is presented in Fig. 10. The results indicated in this figure were based on calculations performed using USPP-PW91 method. In this diagram, the reference energy is taken as the sum of energies for the isolated slab and of $CO(g)+2H_2(g)$ molecules in gas phase. From this diagram it can be seen that both dissociation of H_2 and CO molecules correspond to exoenergetic processes on the

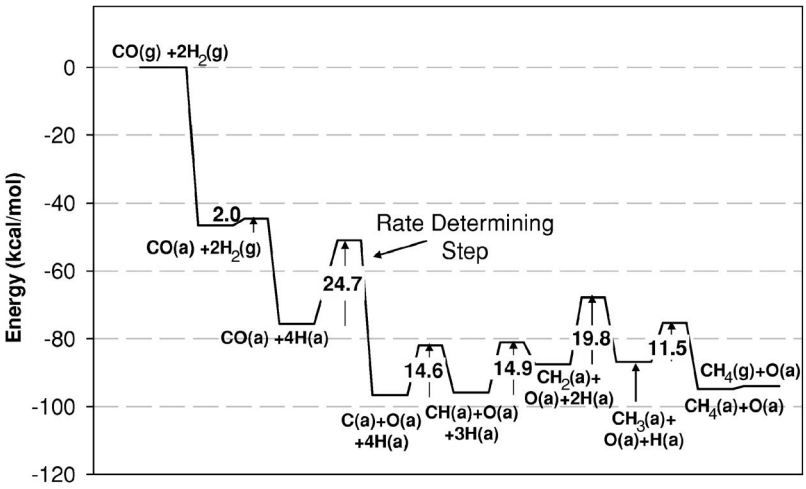

FIG. 10. Potential energy diagram for adsorption and dissociation of CO and H_2 species on the Fe(100) surface leading to adsorbed C, H, and O species and to hydrogenation reactions of CH_x species with formation of CH_4. The symbols (a) and (g) of different chemical species denote adsorbed, respectively gas phase species.

Fe(100) surface. Among various intermediates, the adsorption of isolated atomic species, $C(a)+O(a)+4H(a)$ correspond to the most stable configuration, followed by CH formation, $CH(a)+O(a)+3H(a)$. As a result, it can be concluded that adsorbed CH species are the most stable from the CH_x $(x=1,4)$ series. Among the sequential hydrogenation steps leading to CH_4 formation, we note that the first $(C+H\rightarrow CH)$ and second $(CH+H\rightarrow CH_2)$ steps have similar activation energies while the third step $(CH_2+H\rightarrow CH_3)$ has the highest activation energy of 19.8 kcal/mol. Finally, by comparing the barrier heights for various dissociation or hydrogenation steps, it can be seen that CO dissociation is the rate limiting step with an activation energy of 24.5 kcal/mol.

IV. CONCLUSIONS

We have performed plane-wave DFT calculations using the USPP-PW91 method to determine the adsorption and diffusion properties of CH_x $(x=0,4)$ species on the Fe(100) surface and have mapped the minimum energy potential paths for hydrogenation reactions of CH_x species leading to CH_4 formation. The main conclusions of this study can be summarized as follows:

(a) At low coverages, C adsorption takes place at hollow $4F$ sites while at 0.5 ML, a $c(2\times2)$ pattern is formed. By the increase in C coverage above 1 ML, all hollow sites are occupied followed by adsorption at bridge sites. Over the coverage range 0.11–2 ML, the C binding energy decreases from 189.7 kcal/mol at 0.11 ML to 164.2 kcal/mol at 2 ML and has a slight increase at 0.5 ML corresponding to the $c(2\times2)$ structure. Above 1 ML, a carbon layer starts to form as a result of direct C-C bonding. This layer practically covers the surface Fe atoms such that direct interaction of gaseous systems with the metal surface is significantly hindered.

(b) In addition to adsorption at surface sites, atomic C can also absorb at subsurface sites in a octahedral configuration. We have identified two octahedral-like subsurface sites in the first subsurface layer positioned below the surface atoms ($S1$ configuration) and below $2F$ surface sites ($S2$ configuration). In both these two cases, absorption is exothermal relative to the bare surface and isolated carbon atom. For the most stable subsurface site $S1$, we have characterized the dependence of the binding energy on coverage and have shown that the maximum is reached at 0.5 ML, similar to the trend found for C adsorption on the surface.

(c) From the surface sites, the C atom can diffuse to the subsurface and further to the bulk. The largest barrier was obtained for the initial step corresponding to diffusion from the surface to the immediate subsurface site with a value of 31.1 kcal/mol. Once the C atom reaches the second layer, further diffusion within the same layer or toward the bulk is possible with much lower activation energies.

(d) Surface site selectivity for the binding of CH_x $(x=1,4)$ species has been determined on the Fe(100) surface in the regime of low coverages at 0.11–0.25 ML. It has been determined that both CH and CH_2 species will bind preferentially at the $4F$ hollow site while CH_3 species will bind in a bridge $2F$ configuration. At 0.25 ML, the corresponding binding energies were found to be 158.2, 99.6, and 43.7 kcal/mol, respectively; while at 0.11 ML, these energies increase slightly to 159.6, 101.5, and 45.8 kcal/mol. The barrier heights for diffusion of CH and CH_2 species among $4F$ sites were determined to be 33.2 kcal/mol and 13.5 kcal/mol, respectively. The corresponding diffusion pathways involve passing through a bridge $2F$ configuration. In the case of CH_3 species, diffusion among $2F$ sites was found to take place with a much smaller barrier of 4.0 kcal/mol and involves a pathway through a $1F$ site. Finally, the CH_4 molecule was found to interact weakly with the iron surface as reflected by its small binding energies with a maximum of 0.9 kcal/mol.

(e) The analysis of the adsorption results for atomic and molecular species, i.e., H, C, O, CH_x $(x=1,3)$ and CO, based on calculations performed using the PAW-PBE method has shown that the calculated binding energies have similar values to those obtained using the USPP-PW91 method. The overall differences among these two sets of values were found in the range −1.4–4.7% with the largest variations corresponding to adsorption of C (2.1%) and CO (4.7%) species.

(f) The presence of C atoms adsorbed at surface and subsurface sites generally leads to an increase in stabilization of other coadsorbed H, C, O, CO, and CH_x surface species. In

TABLE VII. The list of vibrational frequencies obtained for different atomic and molecular species adsorbed on the Fe(100) surface at different coverages θ, as determined within frozen phonon approximation based on USPP-PW91 calculations.

System/Site[a]	θ	ν_1	ν_2	ν_3	ν_4	ν_5	ν_6	ν_7	ν_8	ν_9	ν_{10}	ν_{11}	ν_{12}
C													
1*F*(1)	0.25	857.6	18.1 i	29.9 i									
2*F*(1)	0.25	868.6	269.3	98.5									
2*F*(4)	1.00	628.5	555.3	340.0									
4*F*(1)	0.25	482.8	482.4	470.5									
4*F*(2)	0.50	500.7	433.8	433.6									
4*F*(4)	1.00	498.7	498.5	484.2									
4*F*(4)-1*F*(1)	1.25	896.9	202.4	202.1									
4*F*(4)-1*F*(4)	2.00	860.4	192.6	192.1									
4*F*(4)-2*F*(1)	1.25	1051.4	517.3	495.4									
4*F*(4)-2*F*(4)	2.00	1115.0	700.9	497.1									
*S*1(1)	0.25	125.4	91.2	78.2									
*S*1(4)	1.00	557.1	481.2	457.2									
*S*2(1)	0.25	934.0	414.0	340.9									
CH													
1*F*	0.25	3081.0	808.5	608.6	607.0	40.3	30.6						
2*F*	0.25	2873.6	714.9	623.2	313.9	241.9	51.9 i						
4*F*	0.25	2919.6	459.5	456.9	447.2	373.7	372.8						
CH_2													
1*F*	0.25	3082.6	2995.0	1281.1	701.6	562.2	440.8	123.3	89.7	47.9 i			
2*F* (pl)	0.25	2925.4	2853.2	1261.8	511.8	424.2	259.5	167.4	53.6	311.7 i			
2*F* (pp)	0.25	3012.2	2938.4	1259.8	581.4	493.8	461.9	380.8	339.3	106.1			
4*F*	0.25	2633.4	2615.3	1212.5	686.7	481.3	367.4	362.0	328.5	285.0			
CH_3													
1*F*	0.25	3050.7	3040.3	2953.9	1377.2	1367.4	1068.7	494.8	484.1	410.5	91.9	13.0	17.4 i
2*F* (pp)	0.25	3037.4	2919.0	2868.0	1376.6	1344.7	1131.3	555.3	425.8	342.6	205.5	105.5	27.4
2*F* (pl)	0.25	3011.1	2953.8	2821.7	1386.6	1332.1	1149.1	543.9	481.8	352.7	166.9	105.9	85.3

[a]Notations 1*F*, 2*F*, and 4*F* indicate the onefold, twofold, and fourfold adsorption sites, respectively; while the number in parentheses indicates the number of species in the supercell adsorbed at the respective surface site. Labels *S*1 and *S*2 refer to the subsurface absorption sites of the C atom as described in text. The acronyms (pl) and (pp) denote parallel and perpendicular configurations, respectively, described in text for CH_2 and CH_3 species.

the case of subsurface C, the stabilizing effect upon the other atomic or molecular adsorbed species was found to increase with the coverage of subsurface C atoms.

(g) The presence of adsorbed C and CH_x species was found to have a strong influence on the magnetic properties of the surface leading to the reduction of the magnetic moments. This effect is the strongest for the case of C atoms and decreases for CH_x species with the increase in the number of H atoms. The demagnetization effects have been found to be mainly localized upon the Fe atoms involved in direct bonding.

(h) The minimum energy paths for successive hydrogenation reactions $C \rightarrow CH \rightarrow CH_2 \rightarrow CH_3 \rightarrow CH_4$ has been analyzed and it has been determined that all these reaction steps are endothermal with exception of the last step leading to CH_4 formation which is exothermal. Among these processes, the largest activation energy was found to correspond to hydrogenation reaction of CH_2 with an activation energy of 19.8 kcal/mol.

(i) Overall, for the ensemble of elementary processes involving adsorption and dissociation of CO and H_2 species, followed by CH_x hydrogenation reactions with CH_4 formation, it was found that the rate determining step corresponds to CO dissociation with an activation energy of 24.7 kcal/mol. Additionally, among different CH_x intermediates on the surface the isolated C and CH species adsorbed at hollow sites were found to be the most stable.

ACKNOWLEDGMENTS

We gratefully acknowledge the computational resources provided by Pittsburgh Supercomputer Center and ARL MSRC supercomputer center.

APPENDIX

Table VII lists the vibrational frequencies for different atomic and molecular species.

[1] *Handbook of Heterogeneous Catalysis*, edited by G. Ertl, H. Knözinger, and J. Weltkamp (Weinheim, VCH, 1997).
[2] G. A. Somorjai, *Introduction to Surface Chemistry and Catalysis* (Wiley, New York, 1994).
[3] F. Fischer and H. Tropsch, Res. Commun. Inst. Ferment **4**, 276 (1923); R. B. Anderson, *The Fischer-Tropsch Synthesis* (Academic, Orlando, FL, 1984).
[4] D. W. Moon, D. J. Dwyer, and S. L. Bernasek, Surf. Sci. **163**, 215 (1985); D. W. Moon, S. L. Bernasek, J. P. Lu, J. L. Gland, and D. L. Dwyer, Surf. Sci. **184**, 90 (1987).
[5] D. W. Moon, S. Cameron, F. Zaera, W. Eberhardt, R. Carr, S. L. Bernasek, J. L. Gland, and D. J. Dwyer, Surf. Sci. **180**, L123 (1987).
[6] J. Benziger and R. J. Madix, Surf. Sci. **94**, 119 (1980); J. Benziger and R. J. Madix, Surf. Sci. **115**, 279 (1982).
[7] M. L. Burke and R. J. Madix, Surf. Sci. **237**, 20 (1990).
[8] P. B. Merrill and R. J. Madix, Surf. Sci. **347**, 249 (1996).
[9] S. K. Nayak, M. Nooijen, S. L. Bernasek, and P. Blaha, J. Phys. Chem. B **105**, 164 (2001).
[10] D. C. Sorescu, D. L. Thompson, M. M. Hurley, and C. F. Chabalowski, Phys. Rev. B **66**, 035416 (2002).
[11] D. E. Jiang and E. A. Carter, Surf. Sci. **570**, 167 (2004).
[12] A. Stibor, G. Kresse, A. Eichler, and J. Hafner, Surf. Sci. **507**, 99 (2002).
[13] D. E. Jiang and E. A. Carter, Surf. Sci. **547**, 85 (2003).
[14] D. E. Jiang and E. A. Carter, Phys. Rev. B **70**, 064102 (2004).
[15] D. C. Sorescu, Catal. Today **105**, 44 (2005).
[16] M. Eder, K. Terakura, and J. Hafner, Phys. Rev. B **64**, 115426 (2001).
[17] D. E. Jiang and E. A. Carter, Phys. Rev. B **71**, 045402 (2005).
[18] I. M. Ciobîca, Ph.D. thesis, Eindhoven University of Technology, 2002 (unpublished); Z. Pan and P. Hu, J. Am. Chem. Soc. **124**, 11568 (2002).
[19] G. A. Morgan Jr., D. C. Sorescu, T. Zubkov, and J. T. Yates Jr., J. Phys. Chem. B **108**, 3614 (2004).
[20] M. Neurock, Top. Catal. **9**, 135 (1999).
[21] X.-Q. Gong, R. Raval, and P. Hu, J. Chem. Phys. **122**, 024711 (2005).
[22] M. Mavrikakis and A. A. Gokhale, Abstr. Pap. - Am. Chem. Soc. **229**, U861 (2005).
[23] G. Kresse and J. Hafner, Phys. Rev. B **48**, 13115 (1993).
[24] G. Kresse and J. Furthmüller, Comput. Mater. Sci. **6**, 15 (1996).
[25] G. Kresse and J. Furthmüller, Phys. Rev. B **54**, 11169 (1996).
[26] D. Vanderbilt, Phys. Rev. B **41**, R7892 (1990).
[27] G. Kresse and J. Hafner, J. Phys.: Condens. Matter **6**, 8245 (1994).
[28] E. G. Moroni, G. Kresse, J. Hafner, and J. Furthmüller, Phys. Rev. B **56**, 15629 (1997).
[29] J. P. Perdew, J. A. Chevary, S. H. Vosko, K. A. Jackson, M. R. Pederson, D. J. Singh, and C. Fiolhais, Phys. Rev. B **46**, 6671 (1992).
[30] P. E. Blöchl, Phys. Rev. B **50**, 17953 (1994).
[31] G. Kresse and D. Joubert, Phys. Rev. B **59**, 1758 (1999).
[32] S. H. Vosko, L. Wilk, and M. Nusair, Can. J. Phys. **58**, 1200 (1980).
[33] J. P. Perdew, K. Burke, and M. Ernzerhof, Phys. Rev. Lett. **77**, 3865 (1996).
[34] H. J. Monkhorst and J. D. Pack, Phys. Rev. B **13**, 5188 (1976).
[35] M. Methfessel and A. T. Paxton, Phys. Rev. B **40**, 3616 (1989).
[36] G. Kresse and J. Hafner, Phys. Rev. B **47**, R558 (1993).
[37] H. Jónsson, G. Mills, and K. W. Jacobsen, in *Classical Quantum Dynamics in Condensed Phase Simulations*, edited by B. J. Berne, G. Ciccotti, and D. F. Coker (World Scientific, Singapore, 1998), p. 385.
[38] C. Kittel, *Introduction to Solid State Physics* (Wiley, New York, 1996).
[39] *CRC Handbook of Chemistry and Physics*, 67th ed. edited by D. R. Lide (CRC, Boca Raton, FL, 1983).
[40] J. A. Montgomery, Jr., J. W. Ochterski, and G. A. Petersson, J. Chem. Phys. **101**, 5900 (1994); S. J. Blanksby and G. B. Ellison, Acc. Chem. Res. **36**, 255 (2003).
[41] V. Blum, A. Schmidt, W. Meier, L. Hammer, and K. Heinz, J. Phys.: Condens. Matter **15**, 3517 (2003).
[42] G. Panzner and W. Diekmann, Surf. Sci. **160**, 253 (1985).
[43] D. E. Jiang and E. A. Carter, Phys. Rev. B **67**, 214103 (2003).
[44] W.-H. Huang and S. L. Bernasek, Surf. Sci. **339**, 272 (1995).
[45] S. Ohnishi, A. J. Freeman, and M. Weinert, Phys. Rev. B **28**, 6741 (1983).
[46] D. Spišák and J. Hafner, Phys. Rev. B **64**, 094418 (2001).
[47] S. D. Cameron and D. J. Dwyer, Langmuir **4**, 282 (1988).